Ionospheric ion temperature climate and upper atmospheric long-term cooling

Citation: Zhang, Shun-Rong et al. "Ionospheric Ion Temperature Climate and Upper Atmospheric Long-Term Cooling: UPPER ATMOSPHERIC COOLING." Journal of Geophysical Research: Space Physics 121.9 (2016): 8951–8968.

As Published: http://doi.org/10.1002/2016JA022971

Publisher: American Geophysical Union (AGU)

Persistent URL: http://hdl.handle.net/1721.1/107625

Version: Author's final manuscript: final author's manuscript post peer review, without publisher's formatting or copy editing

Ionospheric ion temperature climate and upper atmospheric long-term cooling

Shun-Rong Zhang[1], John M. Holt[1], Philip J. Erickson[1],

Larisa P. Goncharenko[1], Michael J. Nicolls [2], Mary McCready[2], and

John Kelly[2]

[1]Haystack Observatory, Massachusetts Institute of Technology, Westford,

Massachusetts, USA.

[2] Center for Geospace Studies, SRI International, Menlo Park, California,

USA.

KEY POINTS:

Ionospheric ion temperature climate for multiple solar cycles using up-to-date IS radar observations in high and midlatitudes

Comparable and consistent altitude dependence of long-term trends among these sites; above 275 km strongly dependent on magnetic latitude

The lower F region (< 275 km) dayside cooling trends significantly higher than anticipated from anthropogenic increase of greenhouse gases

---

Corresponding author: **S.-R. Zhang**, Haystack Observatory, Massachusetts Institute of Technology, Route 40, Westford, MA 01886 (shunrong@haystack.mit.edu).

Abstract. It is now recognized that Earth's upper atmosphere is experiencing a long-term cooling over the past several solar cycles. The potential impact of the cooling on societal activities is significant, but a fundamental scientific question exists regarding the drivers of the cooling. New observations and analyses provide crucial advances in our knowledge of these important processes. We investigate ionospheric ion temperature climatology and long-term trends using up-to-date large and consistent ground based datasets as measured by multiple incoherent scatter radars (ISRs). The very comprehensive view provided by these unique observations of the upper atmospheric thermal status allows us to address drivers of strong cooling previously observed by ISRs. We use observations from two high latitude sites at Sondrestrom (Invariant latitude 73.2°N) from 1990-2015, and Chatanika/Poker Flat (Invariant latitude 65.9°N) over the span of 1976-2015 (with a gap from 1983-2006). Results are compared to conditions at the mid-latitude Millstone Hill site (Invariant latitude 52.8°N) from 1968-2015. The aggregate radar observations have very comparable and consistent altitude dependence of long-term trends. In particular, the lower F region (< 275 km) exhibits dayside cooling trends that are significantly higher (-3 to -1K/year at 250 km) than anticipated from model predictions given the anthropogenic increase of greenhouse gases. Above 275 km, cooling trends continue to increase in magnitude but values are strongly dependent on magnetic latitude, suggesting the presence of significant downward influences from non-neutral atmospheric processes.

1. Introduction

It is now recognized that the terrestrial upper atmosphere is experiencing long-term cooling over the last few solar cycles. Compelling evidence for this cooling comes from direct measurements of long-term decreases in both thermospheric density [Keating et al., 2000; Emmert et al., 2004, 2008] and ionospheric temperature [Zhang et al., 2005a; Holt and Zhang, 2008; Zhang et al., 2011; Ogawa et al., 2014] which are indicative of corresponding neutral temperature variations [Oliver et al., 2014]. Other indirect but relevant observations include a lowering of the ionospheric F2-layer altitude, an increase in the F1 region electron density, and other ionospheric changes, as reviewed, for example, in Laštovička et al. [2006, 2012]; Qian et al. [2011]; Cnossen [2012]; Danilov [2012]. We note that some of these results come from ionosonde-based studies and therefore are estimated either roughly (e.g., for hmF2) or subject to large uncertainties [Rishbeth, 1990]. The cooling of the neutral atmosphere and corresponding changes in plasma properties are generally consistent with expected upper atmospheric variations caused by green-house gas increases since the beginning of industrial era, as simulated initially by Roble and Dickinson [1989], and confirmed later by Qian et al. [2006] and Solomn et al [2015].

However, quantitative differences among observations and between simulations and observations of the long-term cooling still exist, raising important questions regarding the most significant driver(s) of climate change at ionosphere and thermosphere altitudes. In general, neutral density decreases from simulation and satellite observations agree reasonably well except for solar minimum conditions, where observational analyses [Emmert et al., 2008; Emmert, 2015] variously show cooling rates that range from moderate to

anomalously strong. Simulations also rely on parameters that are inherently uncertain and difficult to derive from observations. For example, the deactivation rate coefficient for CO_2-O collisional excitation and a reasonable CO_2 mixing ratio in the lower thermosphere are needed in order to produce neutral density trends that are comparable to observations [Solomn et al , 2015]. Oliver et al. [2014] derived [O] long-term trends and found that [O] decreases at 400 km at a rate comparable with satellite drag data based estimates, but increases significantly at 120 km in a manner inconsistent with the latest satellite data estimates [Emmert, 2015].

One outstanding inconsistency among existing modeling and observation results occurs for ion temperature trends. In particular, incoherent scatter radar (ISR) ionospheric ion temperature (T_i) measurements show a long-term cooling much larger than predictions using the simulated effects of CO_2 increases. For example, at Millstone Hill (42.5°N, 288.6°E, Invariant latitude 52.8°N), Zhang et al. [2005a] found a negative T_i trend for most F2 region altitudes over 1978-2002. Holt and Zhang [2008] quantitatively estimated that at 375 km altitude, the long-term cooling rate at noon is -3.6 to -5.8K/year (95% confidence level) for the period 1978-2007. Using a longer dataset spanning the 1968-2006 period for 100-500 km height range, Zhang et al. [2011] determined that the altitude profile of noontime T_i cooling has a secular trend that grows in the topside while changing much less at 200-250 km. The noontime cooling is more significant at low solar activity than at high solar activity. Zhang and Holt [2013] further explored the large variability of the cooling trend in T_i in altitude and time. That study concluded that T_i cooling rates at the topside were exceptionally strong, stayed moderate in the 250-300 km range, and were very large during the day and weak (or even turned toward warming) at night. The

24-hour averaged T_i cooling trend for 250-300 km was $\sim$ -4K/decade during 1968-2006. However, due to large day-night differences and strong altitude dependence, this rate has a large uncertainty.

While the Millstone Hill local T_i cooling rate of -4K/decade is close to but still larger than global simulation predictions, observed strong topside cooling and weak (or even warming) trends at night remain yet to be explained. The strong variability of these trends is not a result of analysis approach deficiencies or issues of data quality, as separate analyses show very similar results [Oliver et al., 2013, 2014]. Rather, the complex nature of ionosphere/thermosphere responses to various drivers from both above and below is the likely driver of significant cooling variability.

The cause of strong ionospheric T_i cooling remains a question under debate [Oliver et al., 2013, 2014; Laštovička, 2015; Oliver et al., 2015]. New results on greenhouse gas CO_2 mixing ratios for the lower thermosphere indicate a faster increase rate than that for surface air [Emmert et al., 2012], and Yue et al. [2015] indicated that the CO_2 mixing ratio increases at up to 12% ppm/decade at 110 km altitude. Therefore, it is possible that strong CO_2 enhancement at the thermobase causes strong ionosphere and thermosphere responses, but to date it is not clear whether this enhanced CO_2 population is of sufficient magnitude to cause the observed trends.

Other plausible drivers for strong cooling include the potential effects of long-term changes in gravity wave activity launched by climate change near the ocean-atmosphere interface [Oliver et al., 2013]. Enhanced gravity wave activity that penetrates into lower and upper atmosphere could then cool the the ionosphere and thermosphere [Yiğit and Medvedev, 2009].

Secular changes in Earth's magnetic fields [Cnossen and Richmond, 2008] may also impact upper atmospheric climate. The observed cooling reported by e.g. Zhang et al. [2011] over Millstone Hill is at a site that is gradually moving further away from the auroral zones where particle precipitation and Joule heating are important energy sources of the ionosphere and thermosphere. The subsequent reduced energy input may contribute to overall ion cooling [Zhang and Holt, 2013].

A final and quite significant possibility lies in the influence of secular changes in solar and geomagnetic activity. ISR-based long term trend analyses should remove the effects of solar cycle dependency, as the T_i dependency on solar flux index (F107) is strongly linear at least for midlatitudes. The geomagnetic activity influence is typically minimized to the degree that was feasible in these ISR studies with the available ionospheric and geomagnetic index data.

This paper adds to previous secular ion temperature studies with a new analysis of high latitude ionospheric climatology emphasizing long-term trends as observed by several ISRs. In particular, we employ data from Sondrestrom (67.0°N, 309.1°E, Invariant latitude 73.2°N), typically located at the cusp during the day, and Chatanika/Poker Flat (65.1°N, 212.6°E, Invariant latitude 65.9°N), often considered as a auroral latitude site. All Sondrestrom observational data available since 1990 through middle 2015 spanning ∼26 years (or 2.5 solar cycles) are used. We note that Ogawa et al. [2014] was able to determine ionospheric F region trends observed with the EISCAT Tromsø radar (69.6°N, 19.2°N, Invariant latitude 66.4°N) using a 33 year data set spanning 1981-2013. Sondrestrom has a similar geomagnetic latitude as Tromsø, but has different geographic latitude and longitude. At the Chatanika/Poker Flat site, the Chatanika ISR conducted observa-

tions for 8 years centered around 1980, with radar observations resuming in 2007 at the Poker Flat ISR (PFISR). The Chatanika/PFISR data is unique and valuable for trend studies due to the large span of data coverage, despite the large data gap. In addition to these two sites, this work updates Millstone Hill ionospheric climatology and long-term trend results with an additional 8 years of observations to form an even larger dataset covering 1968-2015. St. Santin (44.6°N, 222°E, Invariant latitude 42.6°N) ISR data is also processed in this work. With the new analysis presented here, we are able to compare ionospheric trends from 4 ISR sites with different latitudes and longitudes. These comparisons provide not only new evidence of strong ionospheric cooling but also provide information on the spatial variability of the cooling.

2. ISR Data and Trend Detection

We analyzed ISR long-term observations from multiple sites in this study. This type of ISR historical data has been extensively used for ionospheric climatology studies, such as empirical models for all ISRs [Zhang et al., 2005b, 2007], mid-latitude plasma temperature climatology [Zhang et al., 2004; Zhang and Holt, 2004], ionospheric E-region electron density [Doe et al., 2005], as well as long-term trend studies mentioned earlier. The ISR technology and data reduction system do evolve with time, however, the evolution is not expected to influence significantly the trend detection. For instance, the error bars for data in more recent years may be slightly smaller than in earlier years, but there is no reason to anticipate some systematical shifts in measurements (e.g., in T_i). Also changes in the radar data reduction system over time have been applied after careful verification and are all documented in the database system. The long-term datasets are available from the Madrigal distributed data system (http://www.openmadrigal.org). As this study is

interested primarily in local measurements for the E and F regions, we select data between 100–550 km altitude using high elevation (>40°) radar measurements. High elevation was selected to ensure enough data for reliable statistics while the analysis for the vertical direction is not significantly biased by data from very low elevation. Using a variety of transmitted waveforms, these ISRs provide typically ∼50 km height resolution for F region observations, and 5-15 km height resolution for E region observations, all with typical temporal resolutions <∼ 5 minutes.

2.1. Sondrestrom and Chatanika/Poker Flat ISR data

The Sondrestrom ISR was originally located at Chatanika, Alaska but was moved to Greenland in 1983 and has subsequently been taking regular observations. Continuous data are available in the Madrigal/CEDAR database beginning in 1990, and therefore data used in this study span 26 years (1990-2015). Sondrestrom statistical data distribution for T_i measurements in the F-region (200–550 km) is shown in Figure 1. The top panel (a) shows the number of data points in log units as a function of year and UT. On average, the hourly data number is ∼4000/year. The mid-panel (b) shows the number of data points as a function of year and month. On average, the monthly data number is ∼8000/year. The bottom panel (c) shows the number of data points as a function of month and hour. On average, for a given month and hour, there are ∼10,000 data points. These monthly and hourly data are further grouped into 12 height ranges, to allow determination of long-term trends for each of the month-hour-altitude bin. These 12 altitude bins center at 110, 130, 150, 170, 190, 225, 275, 325, 375, 425, 475, and 525 km, respectively. In aggregate, therefore, there are on average ∼800 data points involved in determining the trend for each month-hour-altitude bin.

Figure 1

171 At the Chatanika/Poker Flat site, ISR experiments began in 1971 and ended in early
172 1982, and the available data for the analysis reported here spans 7 years between 1976
173 - 1982. Since the start of the second International Polar Year in 2007 [Zhang et al.,
174 2010], the Poker Flat ISR (PFISR) became fully operational for ionospheric measure-
175 ments. Available data from PFISR for this study spans approximately 9 years since 2007.
176 Therefore at the Chatanika/Poker Flat site, 17 year's worth of data in aggregate were
177 used representing a 40-year span of time. We note that the trend information derived by
178 this analysis is governed largely by the data at the critically important beginning and end
179 of the time span. Nevertheless, the gap between 1984-2006 at Chatanika/Poker Flat is
180 large, and therefore these results have somewhat compromised significance as compared
181 to the more continuous Millstone Hill observational record. Figure 2 is similar to Figure **Figure 2**
182 1 but shows data distribution at Chatanika/Poker Flat.

2.2. Trend Detection

183 A binning and fitting method is used for data processing and trend detection as detailed
184 in Holt and Zhang [2008]; Zhang et al. [2011]; Zhang and Holt [2013]. This method
185 binned data into 24 hourly, 12 monthly, and 12 altitude subsets. For a given height-local
186 time bin, a monthly median was found if there were more than 6 data points. Taking
187 monthly median values was necessary to eliminate observational issues such as outliers,
188 over-sampling, and short-term correlation over hours or days.

189 The resulting processed results for T_i at Sondrestrom are shown in Figure 3, where each **Figure 3**
190 data point is a monthly median for a particular time and altitude bin. From the full
191 results, the figure shows T_i trends at local noon $\pm$ 3 hr data for 7 representative altitude
192 bins. The corresponding F107 and Ap indices are also included. To minimize effects

from extreme solar-geophysical conditions, we have excluded data with F107 $>$ 300 SFU (solar flux unit; 10^{-22} W m^{-2} Hz^{-1}) or with Ap $>$ 80. Very similar to Millstone Hill at midlatitudes [Zhang and Holt, 2013], strong solar activity dependence of T_i exists even at this very high latitude station. This dependence is a dominant feature and makes it possible to deduce a solar cycle independent long-term trend. We therefore proceeded to model T_i variations for each of the local time-altitude bins in terms of F107 and Ap dependence and long-term trend using the equation

$$\begin{aligned} T_i \;=\; & T_b + t(y-\bar{y}) + \sum_{n=1}^{2}\left[a_n \sin(2\pi n d/365) + b_n \cos(2\pi n d/365)\right] \\ & + \; f_1(F107 - \overline{F107}) + f_2(F107 - \overline{F107})^2 \\ & + \; a(Ap - \overline{Ap}) \\ & + \; R \end{aligned} \tag{1}$$

where y is the floating-point year containing the day number of the year information as fraction, $\bar{y}$ is the mean floating-point year for the entire time series, d is the day number of the year, F107 is the daily solar 10.7 cm flux in sfu, $\overline{F107}$ is the mean F107 determined over the entire time series, Ap is the daily Ap index, and $\overline{Ap}$ is the mean Ap value determined over the entire time series. The fitting residual is in the R term. The background constant term T_b, long-term trend t, and F107 and Ap term coefficients f_1, f_2 and a are obtained through least square fitting for each local time-height bin.

This bin-fit modeling approach or its variant has been extensively used previously in ISR-based climatology and long-term trend studies [Zhang et al., 2005b, 2007; Holt and Zhang, 2008; Donaldson et al., 2010; Oliver et al., 2013]. The solar activity F107 dependence term includes a second order polynomial to account for saturation/amplification

effects [Balan et al., 1994; Lei et al, 2005; Liu et al, 2011]. However, the magnetic activity dependence term does not include a second order polynomial mainly because the amount of data for active magnetic conditions (30<Ap<80) is sparse, and thus the study data set primarily covers low to moderate magnetic activity data. The use of Ap index dependence is, however, worth noting. While it generally correlates well with magnetospheric energy inputs to the upper atmosphere, the planetary index Ap, constructed from an average of several magnetic stations, is likely not ideally suited to precisely quantify influences on T_i from magnetic activity at Sondrestrom and Chatanika/Poker Flat. This is true in particular at night when both energetic particle and electromagnetic heating intensities at high latitudes during substorms have complicated correlation with nearly any magnetic activity proxy. Even the AE index, inherently more local to the auroral zone, has issues for the long term trend study reported here if it was used as a primary quantifying index for the overall heating response to geomagnetic activity drivers at different altitudes and for the dayside and nightside ionosphere. The hourly AE index also has some discontinuities over the ISR study time periods used here. Although neither of these indices is ideal, we have used Ap dependence to maintain consistency with previous studies [Holt and Zhang, 2008; Zhang et al., 2011; Zhang and Holt, 2013]. Later in the discussion section, we present results of using an alternative proxy, the Interplanetary Magnetic Field (IMF) north-south component Bz, to approximately evaluate uncertainty of the derived trends when employing a different magnetic activity characterization.

3. Ionospheric ion temperature climatology

The regression procedure applied to each month-hour-altitude bin yields coefficients as well as corresponding terms representing various components of variation. These com-

ponents quantify the dependency on F10.7, Ap, season, and long-term trend, and can be expressed as in regression residual form. For example, the trend residual is defined as $T_i - T_b - \sum_{n=1}^{2} [a_n \sin(2\pi nd/365) + b_n \cos(2\pi nd/365)] - f_1(F107 - \overline{F107}) - f_2(F107 - \overline{F107})^2 - (Ap - \overline{Ap})$ where all the terms are from the regression procedure except for Ti which corresponds to the observation. Similarly the F107 solar flux residual is defined as $T_i - T_b - t(y - \bar{y}) - \sum_{n=1}^{2} [a_n \sin(2\pi nd/365) + b_n \cos(2\pi nd/365)] - (Ap - \overline{Ap})$.

3.1. Sondrestrom

The trend residuals (left panel) are calculated by subtracting from the observational binned data all regression terms except for the trend term. Figure 4 shows Sondrestrom results with trend residuals on the left panel. Gray dots are trend residuals representing data from different hours (i.e., 24 hourly bins included), seasons (i.e., 12 monthly bin included), or years. The red line shows the linear trend determined based on these data points. The trend value is also marked for each altitude panel as a temperature change rate in units of K/year. The blue dots are yearly averages. The results show that cooling trends in the upper F-region are very significant near the F2 peak but less significant below the peak, and change to a warming trend at F1-region altitudes. Trend values are based on data for all hourly bins without separation into dayside and nightside, and therefore represent overall conditions during the time period from 1990-2015. As indicated earlier, the ionospheric T_i trends appear to have local time dependence [Zhang and Holt, 2013], and trend variability will be examined more closely in later sections.

Figure 4

The F107 solar flux residuals (middle panel (b) in Figure 4) are presented in a similar manner. A linear fit (red line in Figure 4b) and a parabolic fit (green line in Figure 4b) are plotted to highlight the F107 influence. Overall, reasonable linearity of the T_i-F107

dependence is quite apparent at Sondrestrom. The change rate of F107 residual over F107, $\delta T_i/\delta f_{107}$, (i.e., the T_i sensitivity to F107 variation) varies with altitude, being the largest around 275-350 km, and smallest at the lowest altitudes (100-120km). Figure 5 shows $\delta T_i/\delta f_{107}$ profiles (the left panel) for the dayside (12±3hr LT) and nightside (00±3hr LT). Results for both the dayside and the nightside are very similar even though the ionosphere for the dayside has solar zenith angles (SZA)∼90° in winter while the nightside can have SRZ <90° in summer. Nevertheless, upper atmosphere "memory" and preconditioning effects help to equalize the daytime and nighttime thermal responses to solar irradiation [Zhang et al., 2011].

Figure 5

The Ap residuals (right panel (c), Figure 4) appear positively correlated with Ap index. The fitted linear slope (red line) shows that T_i is most sensitive to Ap around 300-350 km (with a slope $\delta T_i/\delta a_p$ of 3.4K/Ap); the E region T_i appears not as sensitive with a slope of 0.4K/Ap. The correlation is not entirely robust due to different T_i sensitivity to Ap at different magnetic local times, and the relationship is much stronger on the dayside when Sondrestrom is under polar cusp influences and less so on the nightside. Figure 5 further examines $\delta T_i/\delta a_p$ profiles on the right panel for both dayside and the nightside, and reveals that dayside influences are indeed stronger than the nightside ones throughout E region to F2 region altitudes. For trend detection purposes, however, since the data are binned according to local time, the time-dependent T_i response to Ap should not affect the trend derived for each specific local time bin. Therefore, combining trend data from these individual local time bins to enhance the statistics of the trend result can be done without introduction of a significant bias associated with local time.

3.2. Chatanika/Poker Flat

Similar data processing was applied in our study to Chatanika/Poker Flat data and results are shown in Figure 6. The results indicate strong T_i dependence on F10.7 and Ap, in a manner generally similar to the Sondrestrom results. Taken as a whole, we note that, despite data gaps, trend results from Chatanika/Poker Flat have significant and reliable information on upper atmospheric long-term change.

Figure 6

The slope $\delta T_i/\delta f_{107}$ is small at low altitudes and large at high altitudes, and slope magnitudes are generally larger than at Sondrestrom. Study results on these particular dependencies are more weighted toward data from the recent solar cycle, characterized as an extended solar minimum during 2006-2008 [Emmert et al., 2010; Solomon et al., 2010, 2011]. During this solar minimum period, the F10.7 index does not always track solar EUV variations for some altitudes (see Figure 6 panel (b)). As a result, estimated trend residuals are low during this period, and high immediately following the period. In general, this oscillation is almost insignificant near the F2-peak altitudes (200-350km) but larger near 140-180km in F1 regions. For this latter altitude range, ISR T_i data reduction often has some uncertainty due to the use of a solar activity (and also magnetic activity) independent ion composition model in data fitting procedures. Similar F1-region T_i data uncertainty occurs in the Sondrestrom data as well (Figure 5), and can cause abnormal high frequency oscillations at some altitudes. Even with these effects, however, trend detection does not seem to be significantly affected, as the F-region trend is quite clear primarily due to noticeable differences in T_i between the beginning and the ending segments of the data. In general, ions are clearly warmer during 1976-1983 as compared to 2007-2015. These differences increase with altitude and are quite similar to other

ISR observational data records. Finally, in the E-region, T_i during the two segments are reasonably close to each other.

4. Trend Analysis

We focus in this section on T_i trends derived from regression residuals for each altitude bin, further processed as a fit to a linear trend line as described in the previous section. We present altitude profiles of the trends and discuss how the profiles change from the dayside to the nightside, from solar minimum to solar maximum, and from summer to winter.

4.1. Altitude dependence

Results from different altitude bins yield altitude profiles of T_i trends. We consider E and F1 region data (below 200 km) only during daytime hours, as radar backscatter intensity below 200 km is typically low at night due to low ambient electron density except in cases at higher latitudes of significant particle precipitation enhancing E region and lower F region electron density. Figure 7 shows profiles over Sondrestrom and Chatanika/Poker Flat during daytime (12±3hr LT) and nighttime (0±3hr LT) hours. A clear cooling (negative) trend in the F2 region for both daytime and nighttime is evident over both sites. The F2 region (>200 km) cooling appears to grow with altitude but appears to slow down considerably at ∼400 km on the dayside (325 km on the nightside) over Sondrestrom while continuing to grow in magnitude over Chatanika/Poker Flat. Below 200 km, the daytime trend is warming (i.e. positive secular gradient) mostly in the F1-region over both sites. In general, we find that daytime trends over both sites are very similar in magnitude, but nighttime trends have somewhat different amplitudes.

Figure 7

4.2. Day-night differences and diurnal variations

The long-term trend in T_i shows consistent cooling for both dayside and nightside, but day-night differences are large (Figure 7). At Sondrestrom, F-region cooling (>200 km) is strong during the day, and weaker at night. For instance, the trend at 275 km is ∼-2.7K/year or ∼-2.5%/decade for the dayside, but only ∼-0.8K/year or ∼ -0.8%/decade for the nightside. At Chatanika/Poker Flat, the day-night trend differences are large in magnitude as are Sondrestrom results, but Chatanika/Poker Flat trends are opposite in sign, as they show less cooling during the day and more cooling at night. Figure 8 shows the detailed diurnal variation of the trends. It appears that the smallest dayside cooling occurs at in pre-noon local times, close to MLT noon (∼1100hr local time) for Sondrestrom, while Chatanika/Poker Flat has the smallest dayside cooling for post-noon local times, close to MLT noon (∼ 1400hr local time).

Figure 8

4.3. Seasonal variation

Our analysis shows that T_i undergoes clear seasonal variations primarily due to solar zenith angle control. At Sondrestrom, the monthly background term T_b over a 24 hour day is generally lower in winter than in summer, and is the largest in April -June (Figure 9, top panels). The derived T_i trends exhibit a semi-annual variation with cooling being strong in equinox and no clear winter-summer differences. This raises the question of whether the derived seasonal variation of the trends arises from residual magnetic activity influence, due to the more frequent occurrence of magnetic disturbances in equinox, the RussellMcpherron effect [Russell and McPherron, 1973]

Figure 9

At Chatanika and Poker Flat, median T_i is generally lower than the corresponding Sondrestrom T_i and exhibits a maximum in July. This seasonal pattern is similar to that

in Tromsø[Zhang et al., 2005b]. The seasonal variation of the trends has a primary annual component, with more cooling in winter than in summer.

4.4. Solar activity and magnetic activity dependency

To quantify T_i trend dependence on solar flux F107, we binned the trend residuals across an appropriate F107 range given the observational values (Figure 10). We focus here only on Sondrestrom results, as Chatanika/Poker Flat data covers less than 2 solar cycles. The results suggest a nonlinear dependence, but also show a clear tendency toward a relatively weak cooling trend for medium to low solar flux as opposed to medium to high solar flux. In particular, for median to low solar flux at 85<F107<115 SFU, the cooling trend is relatively weak (-4 to -2K/year in the F-region), but for median to high solar flux at 135<F107<200 SFU, the cooling trend is relatively strong (-4 to -7K/year in the F-region). We note in particular that this trend analysis result may be impacted by a potential misrepresentation of T_i dependence on F107 using the model Equation (1). If T_i is over (under) estimated by the model, the T_i trend may appear to have a larger (smaller) cooling value. It is therefore possible that some of the non-linearity seen in the T_i trend with respect to F107 arises mostly from this potential error in T_i dependency. However, we assert that the most reliable trend estimates are for the F107 range 70<F107<150 SFU where the majority of the data resides and therefore where the T_i-F107 relationship is better determined. Within this range, the finding of smaller cooling rates at F107 of 100 to 125 SFU is a particularly strong and consistent signal and a relatively robust finding. This is significantly different from mid-latitude Millstone Hill results where, within this same F107 range, cooling rate magnitudes are in fact the largest [Zhang and Holt, 2013].

Figure 10

Similar analysis of Ap magnetic activity dependence of the trends (Figure 11) show that for very quiet magnetic conditions (Ap<10), the cooling trend is stronger than that for modest to quiet magnetic activity (Ap∼15). These trend findings for very low Ap (-4∼-2K/year) are relatively robust, as they are derived from a much large volume of data and are less contaminated by magnetic disturbance effects. Further discussion on magnetic activity effects on trend detection using a different activity proxy (i.e. IMF Bz) are presented in the next section.

Figure 11

5. Comparing T_i trends from multiple ISRs

In general, ion temperature observations from various ISRs show significant variability in altitude, local time, geomagnetic and solar activity, and even season (to a lesser degree). Some of the observed variability features are common while others may be location dependent, reflecting local factors such as magnetic-geographic latitude offset. In this section, we examine results at multiple geographic locations by comparing high latitude ion temperature trends from Sondrestrom and Chatanika/Poker Flat with mid-latitude trends from Millstone Hill and St. Santin. Results here use the same analysis methods for Millstone Hill data as for high latitude sites described earlier, with the bulk of data previously analyzed and summarized in Zhang and Holt [2013]. However, additional new Millstone Hill observations for 9 years from 2007-2015 are added to the previous data set in this study, and the resulting analysis for Millstone Hill now covers 1968-2015.

Similar analysis is applied to St. Santin data (1966-1987) and the results are also included here. The St. Santin dataset covered only up to 1987 when global warming signals at the surface (e.g. lower atmospheric temperature) had just started, so that these data perhaps represent a different long-term change scenario than at other sites which

all have data to the end of 2015. For this reason, we show St. Santin results only for reference and do not provide further detailed discussions of their trends.

T_i trends derived for all these radars are given in Figure 12. Comparison of these multiple data sets reveals a number of common features that are further explained in following subsections.

Figure 12

5.1. Consistently strong dayside cooling trends in the F region below 275 km

Even though they are located at very different geomagnetic and geographic latitudes, all radars show a cooling trend in the F region on the dayside. At low altitudes (200-275km) where T_i is presumably close to neutral temperature Tn for magnetic quiet conditions, trends from all three sites with data up to 2015 are in close agreement. This result implies: (1) a common driver for long-term cooling, and (2) an association of this driver with neutral atmospheric long-term changes. At 250 km, these cooling trends are -1 to -2 K/year, and are significantly larger than anticipated cooling ($\sim$-0.5K/year) predicted by doubling CO_2 [Qian et al., 2011].

5.2. Increased cooling rates in the topside ionosphere

Cooling rates in the F region increase with altitude from 200 km to at least 425 km. The cooling at 275 km is between -1.5 and -2.75 K/year, and at 375 km is between -2 and -4 K/year. At high altitudes (above 275 km), several factors complicate response. These include energetic processes such as soft particle heating at high latitudes, field-aligned heat flow into the topside ionosphere, and plasmasphere and/or magnetospheric variability. These factors combine to produce a large range of topside ionosphere cooling trends among the three sites.

5.3. Apparent warming in the F1-region

All ISR data sets show an apparent warming trend between 150-200 km. ISR T_i data in the F1-region have some ambiguity in results due to comparable number densities of O^+ and molecular ions. (These conclusions do not apply to the F2-region where O^+ is the dominant species.) This F1 region ion temperature and ion composition ambiguity is typical for regular ISR ion-line spectrum measurements (e.g. Oliver [1979]). Combining ISR plasma-line (accurate Ne) data with the ion-line data allows this ambiguity to be resolved [Waldteufel, 1971; Aponte et al., 2007]. However, for the more general ion-line only ISR product that forms the vast majority of the data sets analyzed here, the ion-line spectrum is sensitive fundamentally to the T_i/m^+ ratio, where m^+ is the total ion mass. Typically model assumptions of ion composition percentage for atomic oxygen O^+ relative to molecular ions are used to set m^+ and therefore allow T_i to be determined. However, long-term changes in thermospheric temperature and composition could potentially cause a long-term change in ion composition percentage relative to O^+ (thus m^+) as anticipated by Roble and Dickinson [1989], and these unmodeled changes could affect the ISR T_i estimation. Based on Millstone Hill data, Zhang et al. [2011] indicated a long-term increase in the F1-region electron density which correlates positively to a hypothesized molecular ion increase. If m^+ does increase, the standard ion composition model underestimates m^+, and therefore the derived T_i underestimates the true T_i. This implies that the T_i observations would have shown an artificial long-term cooling. However, we see a dominant F1-region warming. This suggests that the observed warming is not related to the F1-region T_i ambiguity in the radar data but is rather a geophysical effect. The observed apparent warming shown at fixed altitude is related to the downwelling of the warm

ionosphere as noted previously by several studies [Akmaev et al., 2006; Donaldson et al., 2010; Zhang et al., 2011]. The rapid increase of the background T_i (T_n) with height between 100-200 km (see [Zhang et al., 2011]) appears to be the key reason why the thermal contraction associated subsidence (downwelling) produces the apparent warming only in the F1-region, not the entire F region.

5.4. Main differences in secular temperature trends between sites

We find the following differences in ion temperature secular trends between sites:

1. Large differences exist in the magnitudes of the trends in the topside ionosphere. While between 200 - 275 km the trends are very similar as noted earlier, at higher altitudes cooling is strongest at the highest magnetic latitude (Sondrestrom), lowest at mid latitudes (Millstone Hill), and therefore well organized as a function of magnetic latitude.

2. Above 425 km, Sondrestrom data indicate a tendency towards large reductions in cooling as compared to lower altitudes. This behavior is similar to EISCAT Tromsø results (using dayside data) where the tendency towards smaller cooling rates started at much lower altitudes (325 km) [Ogawa et al., 2014]. This result was also reported in simulations [Qian et al., 2011]. Interestingly, Sondrestrom data indicate that the reduced cooling trend appears more significant on the nightside, as it started at 325 km (Figure 7). On the dayside, this feature begins at 425 km, unlike Tromsø.

3. The causes for reduced T_i cooling trends in the topside ionosphere (>450 km) near the cusp region are not immediately clear. Thermal conduction becomes increasingly important with altitude for electron and ion energy balance, but neutral effects on ion temperature balance, a primary cooling source for the ions, become much less important with altitude due to the rapid fall of neutral density and a subsequent decrease in

ion-neutral collision rates. As a result, T_i should follow T_e more closely than T_i follows T_n, and influences of non-neutral atmospheric origin including those from above (plasmasphere/magnetosphere) should become relatively large. However, this situation is not quite applicable to lower latitudes (Millstone Hill and Chatanika/Poker Flat) where topside heating and thermal conduction for the ions due to influences from above are less significant. Our analysis for the trends in Ne (δNe) and in Te (δTe) (outside of the scope of this paper) suggest that they are both negative (long-term decrease), implying that energy transfer from electrons to the ions via Coulomb collision is also decreasing long-term. It is therefore likely that downward heat flux to the ions must play a significant role.

4. Day-night trend differences in the three stations are somewhat different. At Millstone Hill [Zhang and Holt, 2013], the cooling at night is not as strong as during the day, and there are actually warming trends at some altitudes (200-350 km) at night. At Poker Flat and Sondrestrom, however, there is less day-night difference as compared to Millstone Hill. Sondrestrom diurnal variations are more similar to Millstone Hill results than to variations seen at Poker Flat.

6. IMF Bz influences

We have analyzed observations in previous sections using planetary magnetic Ap index as an activity proxy. The dayside high latitude ionosphere undergoes direct solar wind impact as well as solar irradiation impact in the E and F-region ionosphere even in winter over Sondrestrom, while the nightside high latitude ionosphere is under magnetotail and substorm influences. To examine the sensitivity of trend results to the selection of magnetic influence proxy, we provide in this section analysis using IMF Bz as an activity proxy, since it is the most important measure of solar wind and magnetosphere interac-

tion. Given the complexity of magnetic activity and its influences on the ionosphere at polar cusp and auroral latitudes for the broad altitude range (E and F regions) we are dealing with, IMF Bz is not always an ideal magnetic activity proxy. Nevertheless, We use hourly Bz values and expect some large auto-correlation of the hourly Bz values such that ionospheric responses may be measured with the hourly T_i. Therefore we essentially smooth out influences from transient IMF variations.

We first tested the dependency of T_i on IMF Bz using the same approach as used for Ap ($\delta T_i/\delta Ap$ in Figure 5) except that data is further divided into Bz+ (positive, northward) and Bz - (negative, southward) groups. Figure 13 shows $\delta T_i/\delta Bz$ for both dayside (red) and nightside (blue) with Bz+ (crosses) and Bz- (circles). The results show that T_i responses to Bz+ and Bz- were similar in that |Bz| increases correlated mostly with T_i increases. The response differences were distinct as well. For Bz-, more negative Bz correlated with T_i enhancement, in particular in the topside F region on the dayside, and in the lower F region on the nightside. In the topside region on nightside, however, more negative Bz corresponds to T_i reduction. The T_i response to Bz+ was much weaker than that to Bz-. More positive Bz+ correlated with T_i enhancements, and the nightside response was larger.

Figure 13

The cooling trends derived for Bz+ and Bz- conditions Figure 14 were similar in that increasing Bz+ corresponded to smaller cooling, and decreasing Bz- tended to have smaller cooling as well. These result are consistent with the conclusion that |Bz| has some influence. However, the Bz sign matters as well, since in general cooling trends for Bz- appear stronger than that for Bz+. The trend results for Bz+ influence corresponded to the weakest cooling near Ap=15 (Figure 11), trends for Bz- corresponded to stronger cooling

Figure 14

toward larger Ap (Figure 11), and trends for Bz∼0 corresponded to those at the lowest Ap.

In summary, trend profiles for Bz+ and Bz- can be seen from Figure 15, and were essentially very similar to Figure 12 which is based on Ap. The characteristic consistency of cooling trends below ∼275 km shown in the Ap-based results stayed nearly unchanged in this IMF Bz activity proxy analysis. Results showing increasing cooling with height remained unaltered and cooling magnitudes remained ordered according to geomagnetic latitude, while the tendency of reduced cooling trends above 425 km over Sondrestrom only were well preserved. In general, however, at the two high latitude sites, trend magnitudes for Bz- were larger than those for Bz+.

Figure 15

7. Concluding remarks

We have conducted a comprehensive investigation of ionospheric ion temperature climatology and long-term trends from very large incoherent scatter radar observational datasets at two high latitude sites: Sondrestrom (close to the dayside cusp region; 1990-2015), Chatanika/Poker Flat (the auroral region; 1976-2015 with a gap in 1983-2006). The high latitude long-term trend results were compared to those from the Millstone Hill mid-latitude dataset (1968-2015). Some consistent features for the derived T_i trends were identified along with other important characteristics. These can be summarized as follows:

1. A long-term cooling trend in T_i in the F region ($>$ 200 km) was clearly identified, confirming that the upper atmosphere, including the ionosphere, is cooling and contracting over long periods. We note in particular that these new results used a large range of geomagnetic latitudes. The cooling observed by multiple radars highlights the global nature of upper atmospheric long-term trends.

514 2. Between 200-275km, ionospheric cooling trends were very comparable among the
515 three locations. The consistency of these T_i trends seems to imply a common driver in
516 the neutral atmosphere which experienced long-term and global cooling.

517 3. At 250 km, T_i cooling at noon was between -1 to -3 K/year. In particular, cooling
518 trend estimation based on the use of Ap index was -1 to -2 K/year. This is equivalent to
519 50-100 K reduction over 50 years. These rates of change at noon fall into prior published
520 estimations for this altitude [Zhang et al., 2011; Oliver et al., 2014; Ogawa et al., 2014].
521 The magnitude of this cooling trend is much higher than anticipated neutral atmospheric
522 cooling caused by anthropogenic increase of greenhouse gases based on model simulations
523 Akmaev et al. [2006]; Qian et al. [2006]; Akmaev [2012], and is also higher than satellite
524 drag data-based cooling estimates [Emmert, 2015].

525 4. The puzzling inconsistency between observational and predicted cooling rates in-
526 dicates the need for further investigations in various directions. For example, renewed
527 studies are needed on the topic of greenhouse gas influences including incorporation of
528 new observations of large CO_2 trends in the lower thermosphere [Yue et al., 2015], clarifica-
529 tion of gravity wave influences is needed [Oliver et al., 2013], and further understanding is
530 needed on variability in derived cooling trends from both satellite data and ground-based
531 observations.

532 5. Observed cooling trends were strongly height dependent and trend magnitude gener-
533 ally grew with increasing altitude during the day. Cooling trend amplitude above 275 km
534 also increased with increasing magnetic latitudes. A reduced cooling tendency occurred
535 above 425 km (dayside) or 325 km (nightside) only at Sondrestrom.

6. In the F1 region below 200 km, ionospheric temperature trends tended towards warming in a consistent manner among the three locations.

Acknowledgments. We thank members of the Haystack Observatory Atmospheric Sciences Group for assembling and maintaining the Madrigal Database. The Millstone Hill incoherent scatter radar is supported by the US National Science Foundation (NSF) Geospace Facilities Program under a cooperative Agreement AGS-1242204 between NSF and the Massachusetts Institute of Technology (MIT). This work is also supported by NSF awards AGS-1042569 and AGS-1343056 to MIT. The Poker Flat Incoherent Scatter Radar (PFISR) is operated by SRI International on behalf of the US National Science Foundation under NSF Cooperative Agreement AGS-1133009. The Sondrestrom Upper Atmosphere Research Facility is funded by grant PLR-1445376 from the NSF. The amount of data involved in this study is huge; they are all from the Madrigal database which is openly available by the public at *http://www.openmadrigal.org*. Please contact Dr. Shun-Rong Zhang (shunrong@haystack.mit.edu) for the processed data published in this paper.

References

Aponte, N., M. P. Sulzer, M. J. Nicolls, R. Nikoukar, and S. A. Gonzalez (2007), Molecular ion composition measurements in the F1 region at Arecibo, *J. Geophys. Res.,* 112(A6), doi:10.1029/2006JA012028.

Akmaev, R. A. (2012), On estimation and attribution of long-term temperature trends in the thermosphere, *J. Geophys. Res.,* 117, A09321, doi:10.1029/2012JA018058.

Akmaev, R. A., V. I. Fomichev, and X. Zhu (2006), Impact of middle-atmospheric composition changes on greenhouse cooling in the upper atmosphere, *J. Atmos. Sol. Terr.*

Phys., 68, 1879-1889, doi:10.1016/j.jastp.2006.03.008.

Balan, N., G. J. Bailey, B. Jenkins, P. B. Rao, and R. J. Moffett (1994), Variations of ionospheric ionization and related solar fluxes during an intense solar cycle, *J. Geophys. Res., 99*, 2243-2253.

Cnossen, I., and A.D. Richmond (2008), Modelling the effects of changes in the Earth's magnetic field from 1957 to 1997 on the ionospheric hmF2 and foF2 parameters, *J. Atmos. Sol. Terr. Phys.,* 70, 1512-1524.

Cnossen, I. (2012), Climate change in the upper atmosphere, in *Greenhouse Gases: Emission, Measurement, and Management*, edited by G. Liu, pp. 315336, InTech, Rijeka, Croatia, ISBN 978-953-51-0323-3.

Danilov, A. D. (2012), Long-term trends in the upper atmosphere and ionosphere (a review). Geomagnetism and Aeronomy, 52(3), 271-291. doi:10.1134/S0016793212030036

Doe, R. A., J. P. Thayer, and S. C. Solomon (2005), Incoherent scatter radar measurements and modeling of high-latitude solar photoionization, J. Geophys. Res., 110, A10303, doi:10.1029/2005JA011129.

Donaldson, J. K., T. J. Wellman, and W. L. Oliver (2010), Long-term change in thermospheric temperature above Saint Santin, *J. Geophys. Res.,* 115, A11305, doi:10.1029/2010JA015346.

Emmert, J. T., J. L. Lean, and J. M. Picone (2010), Record-low thermospheric density during the 2008 solar minimum, *Geophys. Res. Lett.,* 37, L12102, doi:10.1029/2010GL043671.

Emmert, J. T., J. M. Picone, J. L. Lean, and S. H. Knowles (2004), Global change in the thermosphere: Compelling evidence of a secular decrease in density, *J. Geophys. Res.,*

109, A02301, doi:10.1029/2003JA010176.

Emmert, J. T., J. M. Picone, and R. R. Meier (2008), Thermospheric global average density trends, 1967–2007, derived from orbits of 5000 near-Earth objects, *Geophys. Res. Lett.,* 35, L05101, doi:10.1029/2007GL032809.

Emmert, J. T., M. H. Stevens, P. F. Bernath, D. P. Drob, and C. D. Boone (2012), Observations of increasing carbon dioxide concentration in Earth's thermosphere, Nat. Geosci., 5, 868871, doi:10.1038/NGEO1626.

Emmert, J. T. (2015), Altitude and solar activity dependence of 19672005 thermospheric density trends derived from orbital drag. J. Geophys. Res. Space Physics, 120, 29402950, doi: 10.1002/2015JA021047.

Holt, J. M., and S. R. Zhang (2008), Long-term temperature trends in the ionosphere above Millstone Hill, *Geophys. Res. Lett.,* 35, L05813, doi:10.1029/2007GL031148.

Keating, G. M., R. H. Tolson, and M. S. Bradford (2000), Evidence of long-term global decline in the Earth's thermospheric densities apparently related to anthropogenic effects, *Geophys. Res. Lett.,* 27, 1523-1526.

Laštovička, J., R.A. Akmaev, G. Beig, J. Bremer, J. Emmert (2006): Global change in the upper atmosphere. *Science*, 314 (5803), 1253-1254.

Laštovička, J., S. C. Solomon, and L. Qian (2012), Trends in the Neutral and Ionized Upper Atmosphere, *Space Sci. Rev.*, 168, 113-145, 10.1007/s11214-011-9799-3.

Laštovička, J. (2015). Comment on Longterm trends in thermospheric neutral temperatures and density above Millstone Hill by W. L. Oliver et al. Journal of Geophysical Research: Space Physics, 120(3), 23472349.

602 Lei, J., Liu, L., Wan, W., and Zhang, S.-R. (2005). Variations of electron density based
603 on long-term incoherent scatter radar and ionosonde measurements over Millstone Hill.
604 Radio Science, 40, RS2008, doi:10.1029/2004RS003106.

605 LiBo Liu, WeiXing Wan, YiDing Chen, HuiJun Le (2011), Solar activity effects of the
606 ionosphere: A brief review, *Chinese Science Bulletin*, 56, 12, 1202

607 Oliver, W. L. (1979), Incoherent scatter radar studies of the daytime middle thermosphere,
608 *Ann. Geophysicae*, 35, 121-139.

609 Oliver, W. L., Zhang, S.-R., and Goncharenko, L. P. (2013). Is thermospheric global
610 cooling caused by gravity waves? Journal of Geophysical Research: Space Physics,
611 118(6), 38983908.

612 Oliver, W. L., Holt, J. M., Zhang, S.-R., and Goncharenko, L. P. (2014). Longterm
613 trends in thermospheric neutral temperature and density above Millstone Hill. Journal
614 of Geophysical Research: Space Physics, 119(9), 79407946.

615 Oliver, W. L., Holt, J. M., Zhang, S.-R., and Goncharenko, L. P. (2015). Reply to comment
616 by Jan Lastovika on Longterm trends in thermospheric neutral temperature and density
617 above Millstone Hill. Journal of Geophysical Research: Space Physics, 120(3), 23502352.

618 Ogawa, Y., Motoba, T., Buchert, S. C., Haggstrom, I., and Nozawa, S. (2014). Up-
619 per atmosphere cooling over the past 33 years. Geophysical Research Letters, 41(15),
620 56295635.

621 Qian, L., R. G. Roble, S. C. Solomon, and T. J. Kane (2006), Calculated and observed
622 climate change in the thermosphere, and a prediction for solar cycle 24, *Geophys. Res.*
623 *Lett.,* 33, L23705, doi:10.1029/2006GL027185.

Qian, L., J. Laštovička, R. G. Roble, and S. C. Solomon (2011), Progress in observations and simulations of global change in the upper atmosphere, J. Geophys. Res., 116, A00H03, doi:10.1029/2010JA016317, [printed 117(A2), 2012].

Russell, C.T., McPherron, R.L., 1973. Semiannual variation of geomagnetic activity. *J. Geophys. Res.,* 78 (1), 92108.

Solomon, S. C., L. Qian, and R. G. Roble (2015), New 3-D simulations of climate change in the thermosphere. J. Geophys. Res. Space Physics, 120, 21832193. doi:10.1002/2014JA020886.

Rishbeth, H. (1999), Chances and changes: The detection of long-term trends in the ionosphere, *Eos Trans.* AGU, 80(49), 590.

Roble, R. G., and R. E. Dickinson (1989), How will changes in carbon-dioxide and methane modify the mean structure of the mesosphere and thermosphere, *Geophys. Res. Lett.,* 16, 1441-1444.

Solomon, S. C., T. N. Woods, L. V. Didkovsky, J. T. Emmert, and L. Qian (2010), Anomalously low solar extreme-ultraviolet irradiance and thermospheric density during solar minimum, *Geophys. Res. Lett.,* 37, L16103, doi:10.1029/2010GL044468.

Solomon, S. C., L. Qian, L. V. Didkovsky, R. A. Viereck, and T. N. Woods (2011), Causes of low thermospheric density during the 20072009 solar minimum,*J. Geophys. Res.,* 116, A00H07, doi:10.1029/2011JA016508.

Waldteufel, P. (1971), Combined incoherent-scatter F1-region observations, *J. Geophys. Res.,* 76(28), 69956999.

Yiğit, E., and A. S. Medvedev (2009), Heating and cooling of the thermosphere by internal gravity waves, Geophys. Res. Lett., 36, L14807, doi:10.1029/2009GL038507.

Yue J., J. Russell III, Y. Jian, L. Rezac, R. Garcia, M. Lopez-Puertas, M. G. Mlynczak (2015), Increasing carbon dioxide concentration in the upper atmosphere observed by SABER, *Geophys. Res. Lett.,* 42, doi: 10.1002/2015GL064696.

Zhang, S.-R., and Holt, J. M. (2004). Ionospheric plasma temperatures during 19762001 over Millstone Hill. Advances in Space Research, 33(6), 963969.

Zhang, S.-R., and Holt, J. M. (2013). Longterm ionospheric cooling: Dependency on local time, season, solar activity, and geomagnetic activity. Journal of Geophysical Research: Space Physics, 118(6), 37193730.

Zhang, S.-R., Holt, J. M., van Eyken, A. P., Heinselman, C., and McCready, M. (2010). IPY observations of ionospheric yearly variations from high- to middle-latitude incoherent scatter radars. Journal of Geophysical Research, 115(A3), A03303. http://doi.org/10.1029/2009JA014327

Zhang, S.-R., J. M. Holt, A. P. van Eyken, M. McCready, C. Amory-Mazaudier, S. Fukao, and M. Sulzer (2005), Ionospheric climatology and model from long-term databases of worldwide incoherent scatter radars, Eos Trans. AGU, 86(18), Jt. Assem. Suppl., Abstract SA52A-03.

Zhang, S.-R., J. M. Holt, A. P. van Eyken, M. McCready, C. Amory-Mazaudier, S. Fukao, and M. Sulzer(2005), Ionospheric local model and climatology from long-term databases of multiple incoherent scatter radars, *Geophys. Res. Lett.,* 32, L20102, doi:10.1029/2005GL023603.

Zhang, S.-R., J. M. Holt, and M. McReady (2007), High latitude convection model based on long-term incoherent scatter radar observations in North America, *J. Atmos. Sol. Terr. Phys.,* 69, 1273-1291, doi:10.1016/j.jastp.2006.08.017.

Zhang, S.-R., J. M. Holt, A. M. Zalucha, and C. Amory-Mazaudier (2004), Mid-latitude ionospheric plasma temperature climatology and empirical model based on Saint Santin incoherent scatter radar data from 1966-1987, *J. Geophys. Res.,* 109, A11311, doi:10.1029/2004JA010709.

Zhang, S.-R., J. M. Holt, and J. Kurdzo (2011), Millstone Hill ISR observations of upper atmospheric long-term changes: Height dependency, *J. Geophys. Res.,* 116, A00H05, doi:10.1029/2010JA016414.

Zhang, S.-R., Holt, J. M., Erickson, P. J., and Goncharenko, L. P. (2015). Daytoday variability and solar preconditioning of thermospheric temperature over Millstone Hill. Journal of Geophysical Research: Space Physics, 120(5), 39133927.

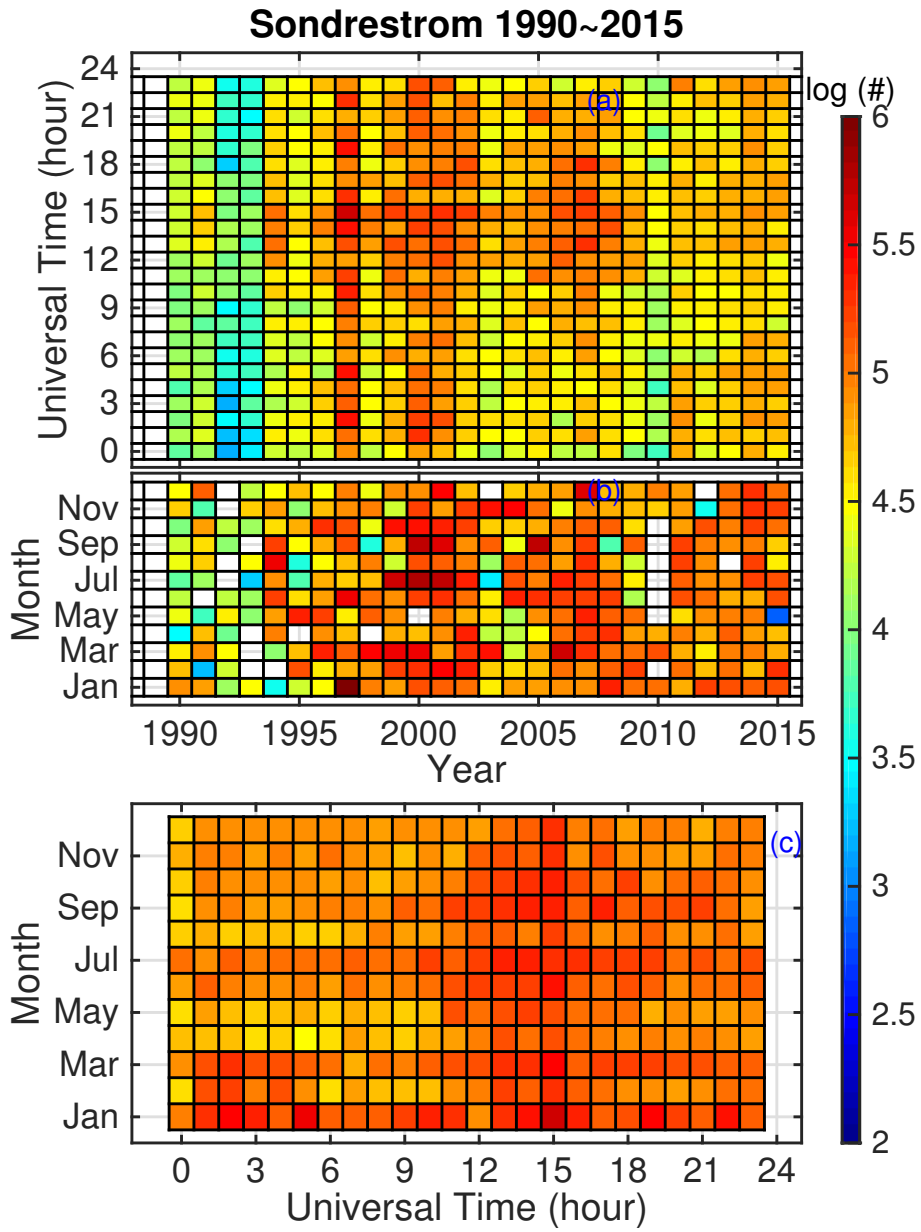

Figure 1. Sondrestrom data distribution at 100–550 km altitude as a function of year and universal time (top panel, a), as a function of year and month (middle panel, b), and as a function of universal time and month (bottom panel, c). The number of data points is shown as a logarithmic value.

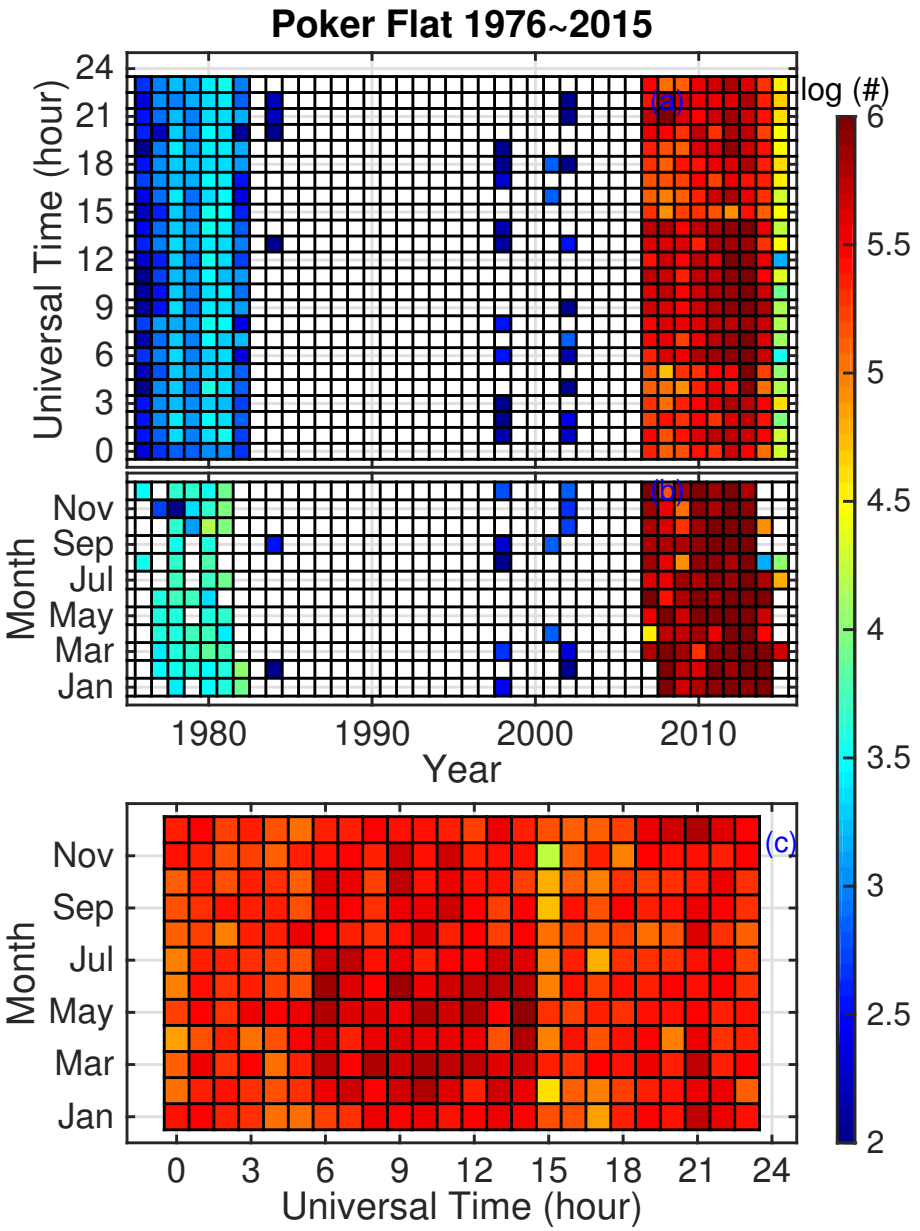

Figure 2. Same as Figure 1 but for the Chatanika/Poker Flat site.

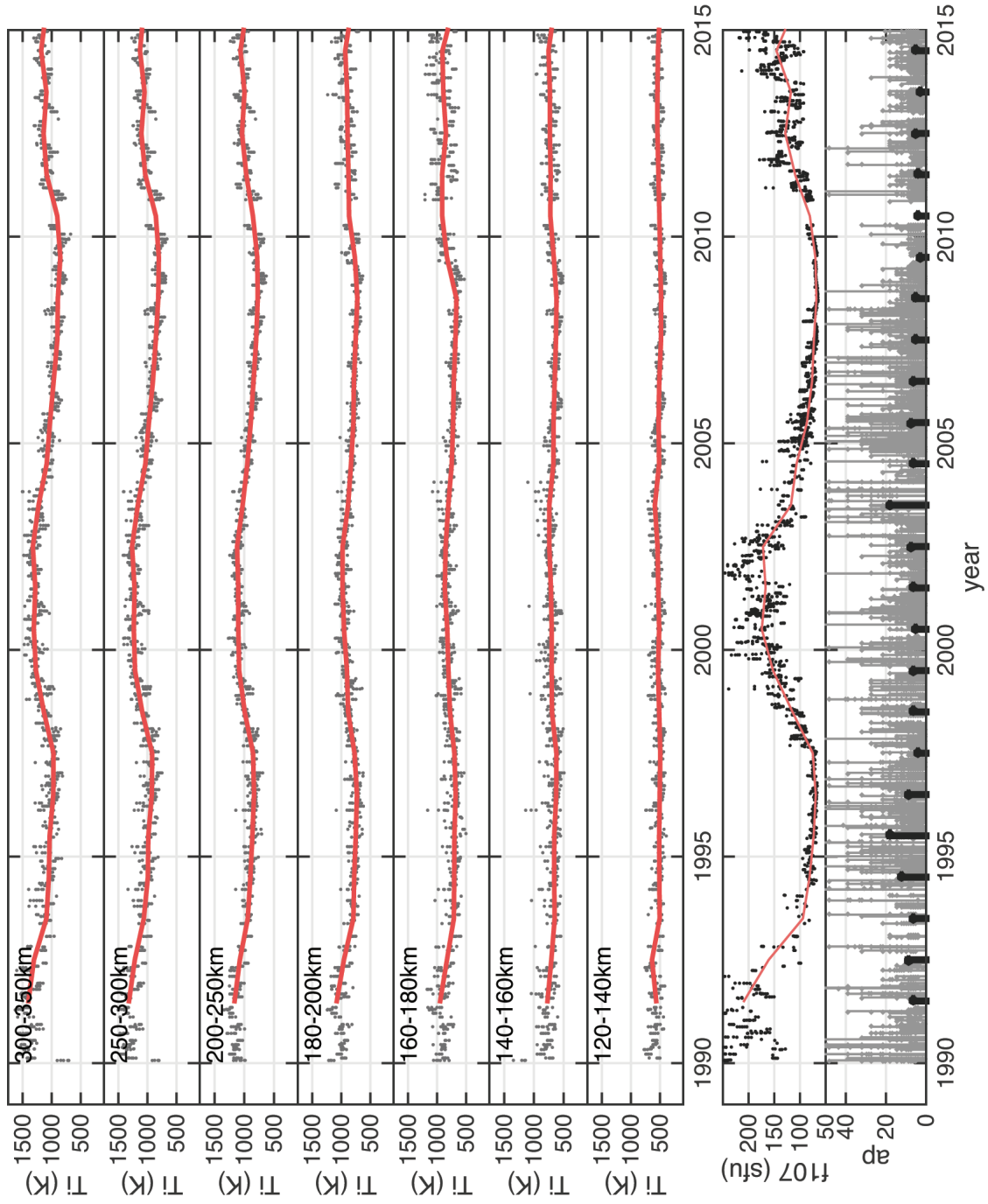

Figure 3. Time series of T_i data for Sondrestrom as monthly and hourly medians at different altitude ranges (top panel), and corresponding F107 (middle panel) and Ap index (bottom panel). Noon time ± 3 hr results are shown. The red solid lines in the top and middle panels and the black bars in the bottom panels are yearly averages.

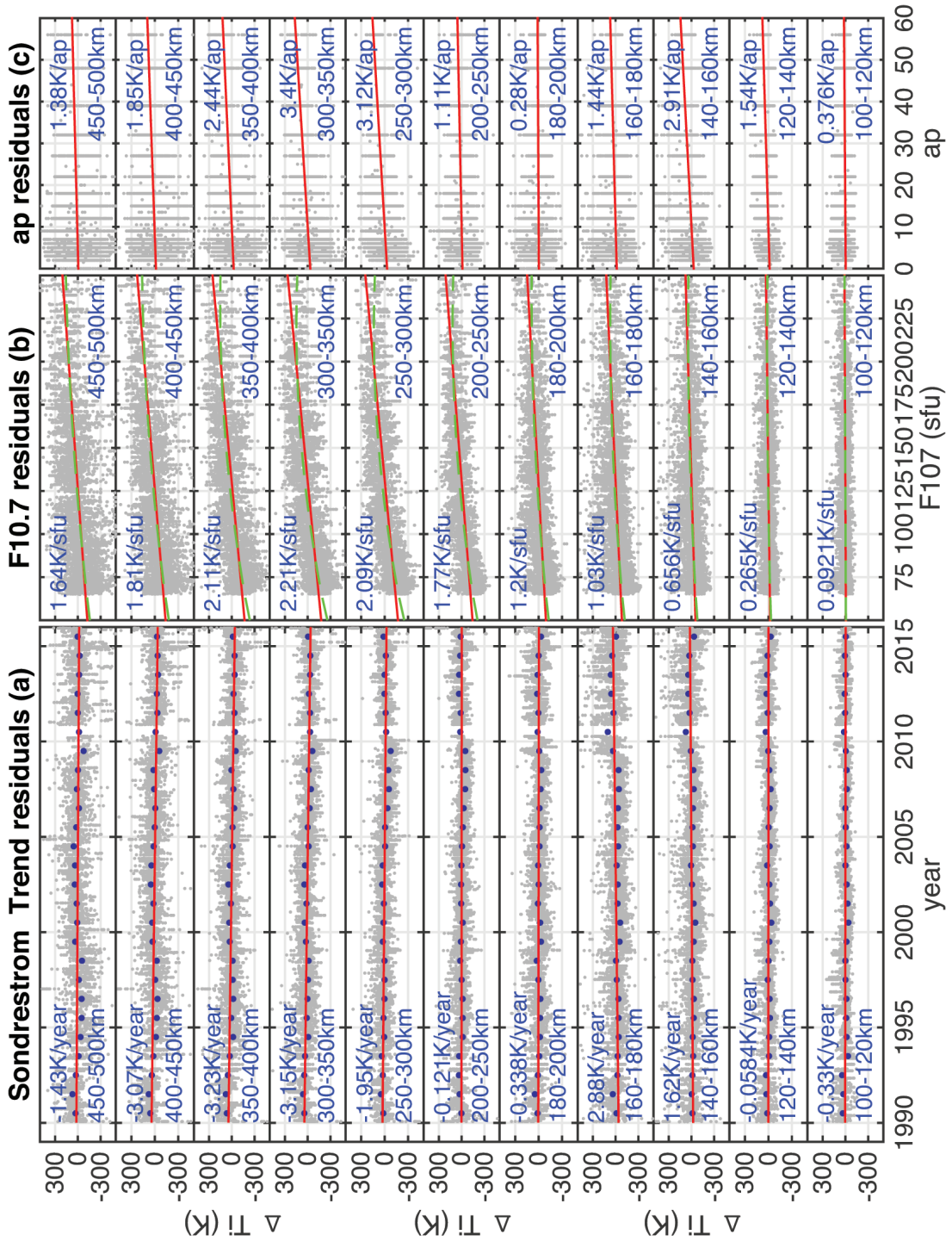

Figure 4. Sondrestrom T_i regression residuals calculated by subtracting geophysical terms in Equation (1) (see text) from the observed data for different altitude bins. Each panel contains hourly and monthly data (gray dots) over the observation period from 1990 through 2015. The trend regression residuals (a) are a result of subtracting all terms except for the trend one, the F107 residuals (b) are a result of subtracting all terms except for the F107 terms, and the Ap residuals are a result of subtracting all terms except for the Ap one. Red lines in each panel are a linear fit to the gray dots; the green line (only in panel b) is a fit to a parabolic function. Solid dark dots (only in panel a) are yearly averages.

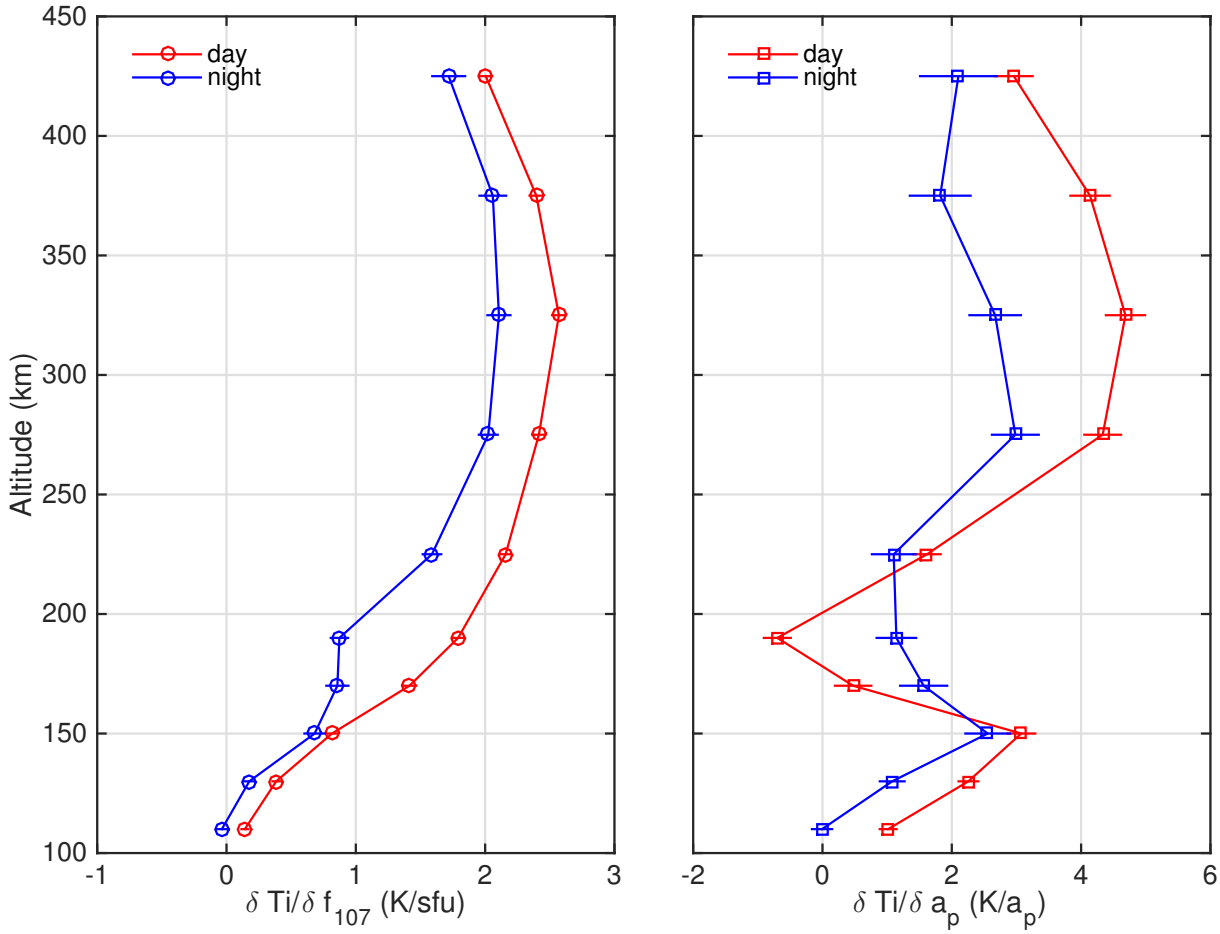

Figure 5. Sondrestrom profiles of T_i trend responses to F107 and Ap, expressed as $\delta T_i/\delta f_{107}$ (left) and $\delta T_i/\delta a_p$ (right) for the dayside (12±3hr LT; red) and the nightside (00±3hr LT; blue).

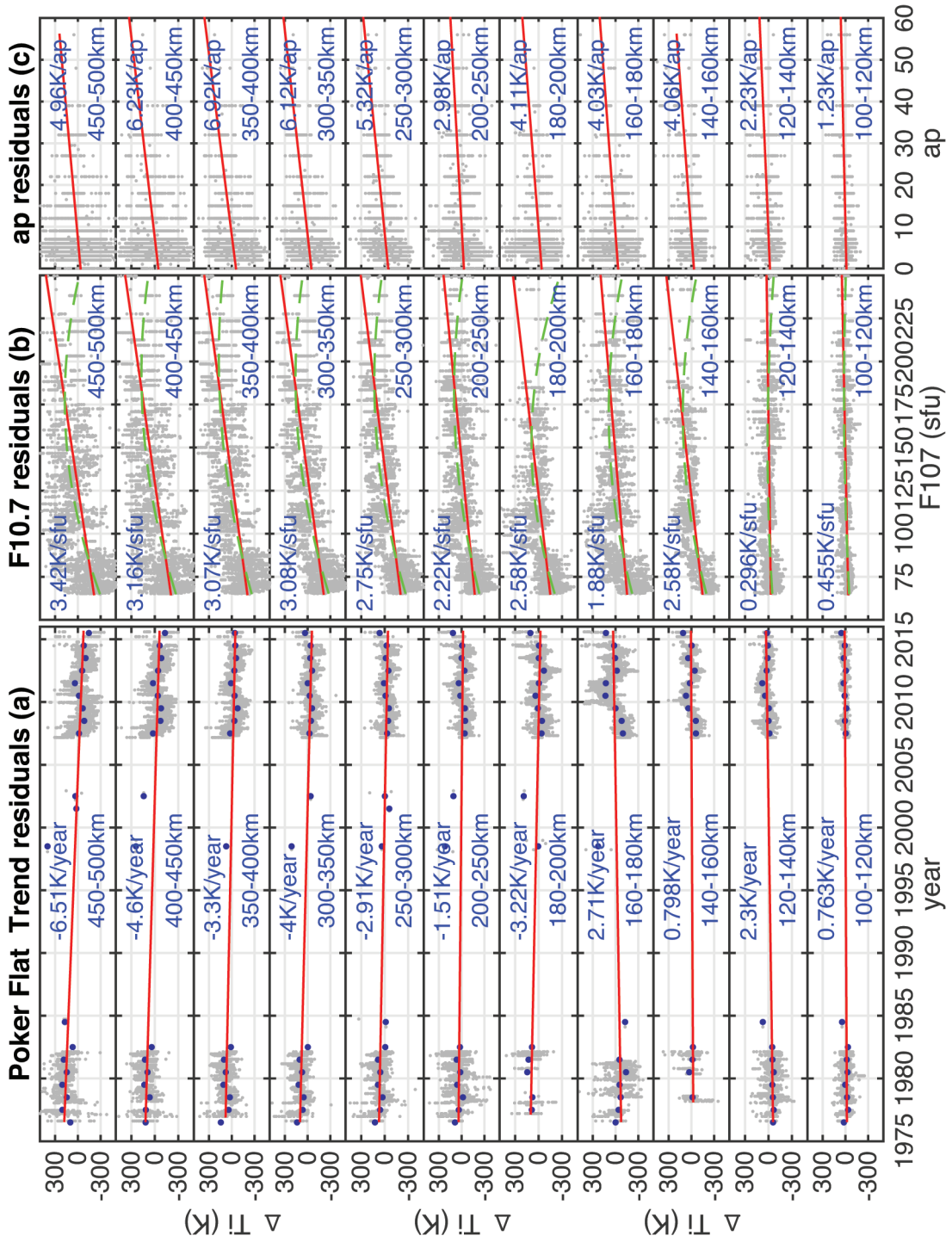

Figure 6. Same as Figure 4 but for Chatanika/Poker Flat over the period 1976 - 2015.

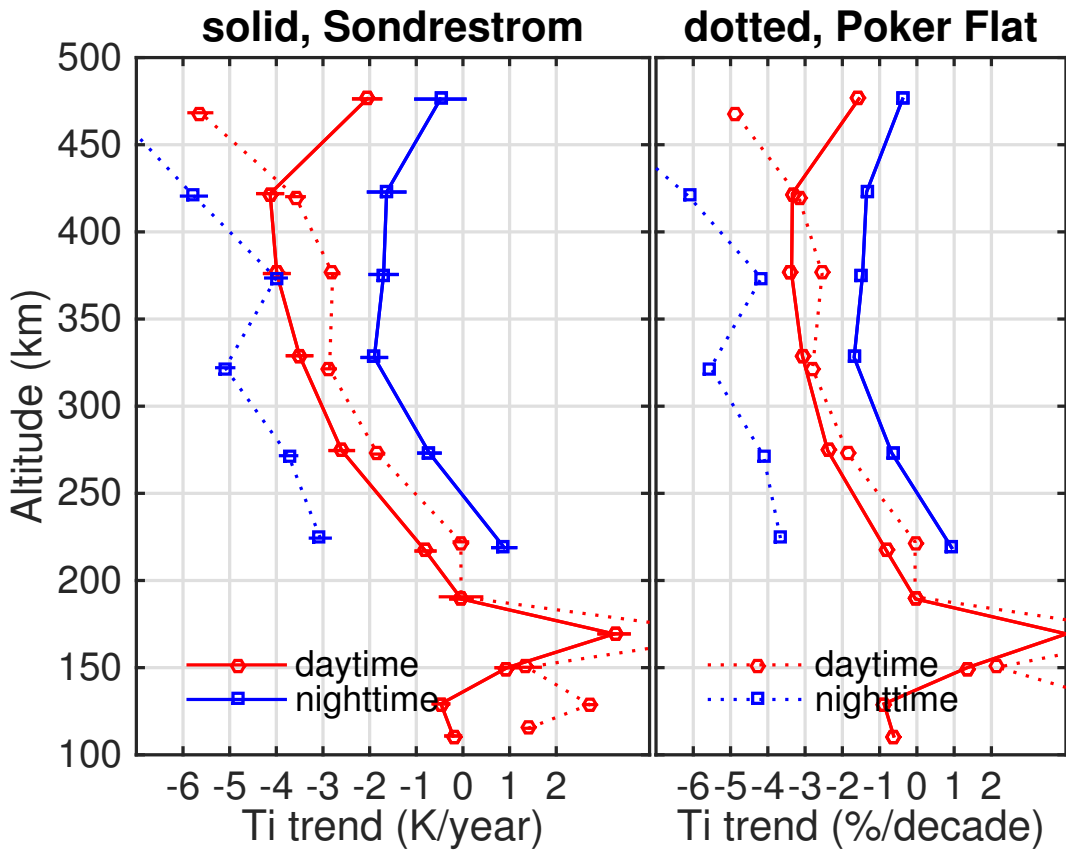

Figure 7. Profiles of T_i trend rates in K/year (left) and in %/decade (right) for the dayside (local noon ±3hr, red) and the nightside (local midnight ±3hr, blue) over Sondrestrom (solid lines) and Chatanika/Poker Flat (dashed lines). Error bars are χ^2-scaled standard deviations for the calculated linear trends.

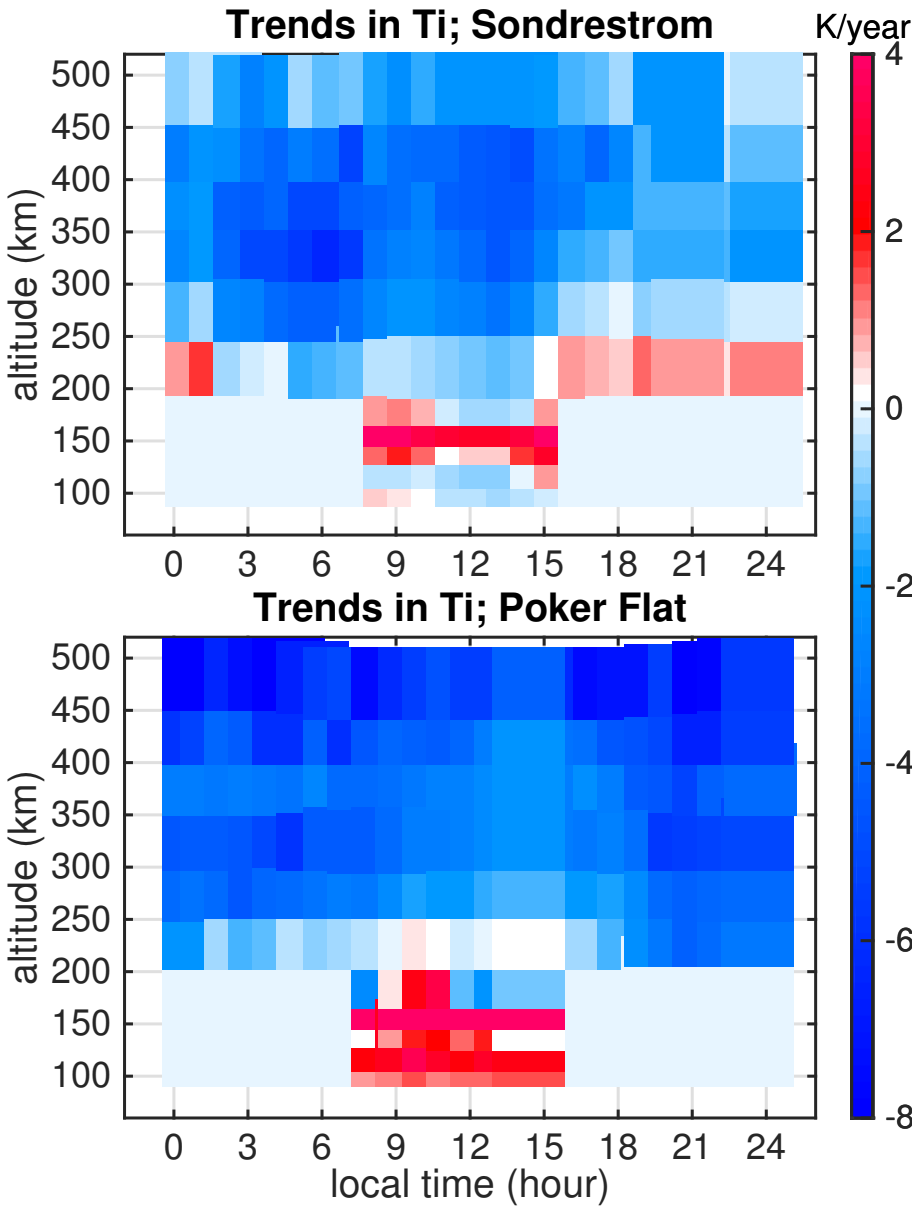

Figure 8. T_i trends as a function of height and local time over Sondrestrom (top) and Poker Flat (bottom).

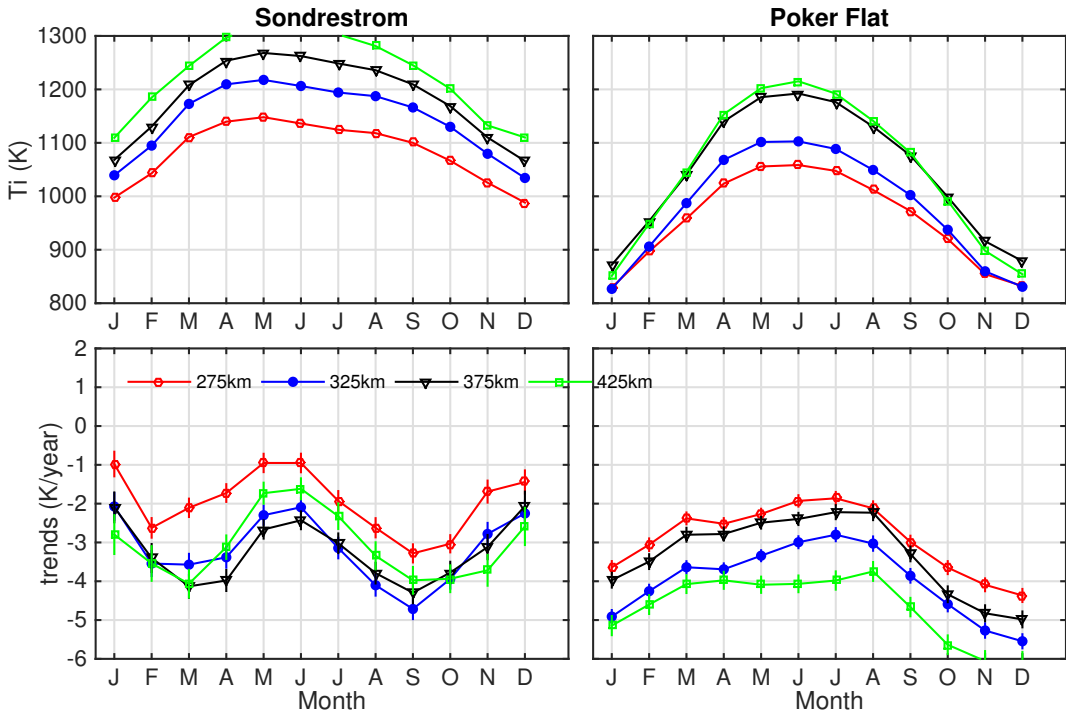

Figure 9. Seasonal variations of median background ion temperature T_b (top) and T_i long term trends (bottom) over Sondrestrom (left) and Poker Flat (right).

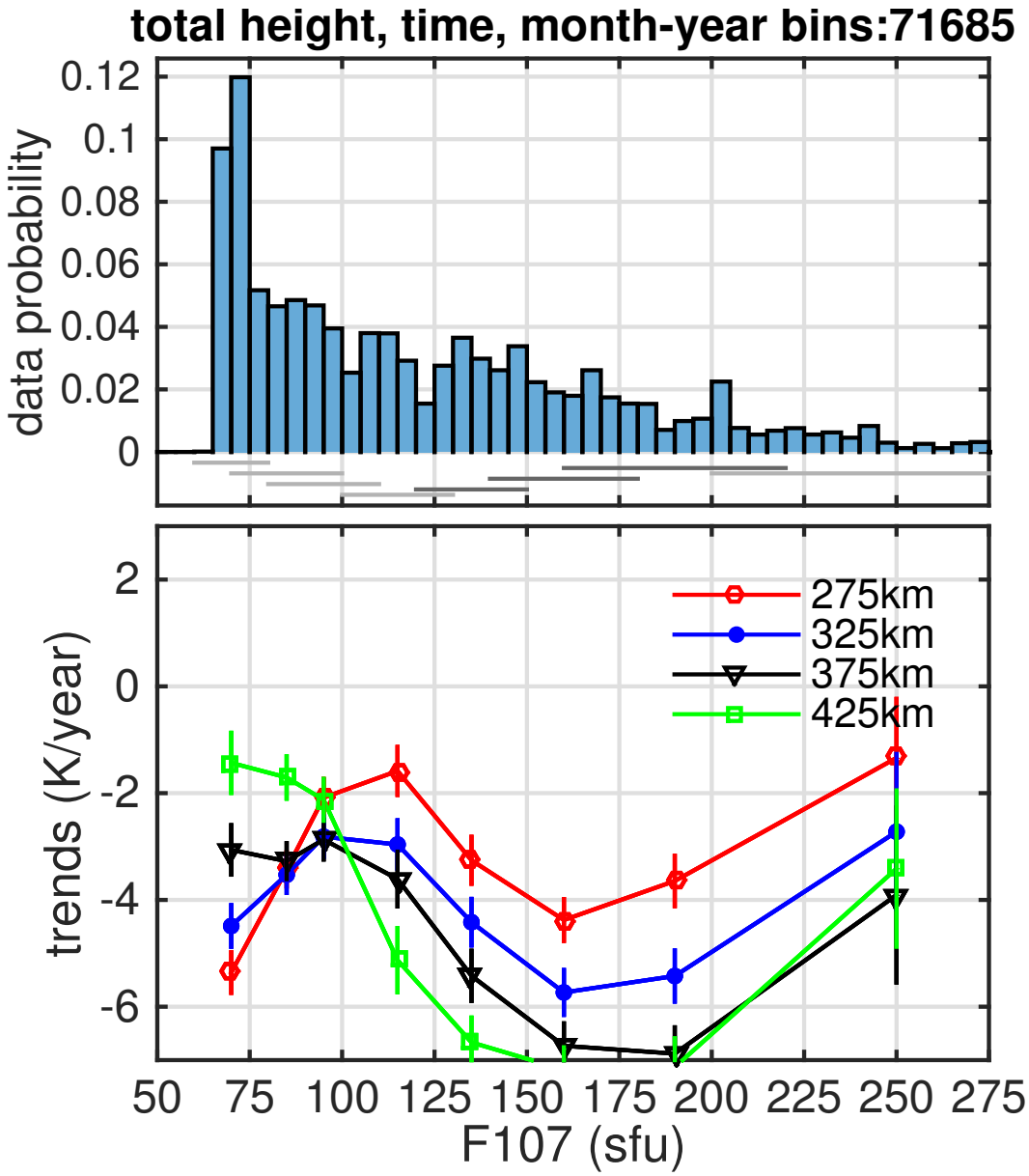

Figure 10. Solar flux F107 dependence of T_i trends for the dayside (local noon ±3 hr) over Sondrestrom. F107 histogram over 5 SFU intervals is plotted in the top panel. T_i trends at different altitudes (bottom) are obtained with binning according to the F107 range as indicated in the horizontal bars (bottom part of top panel). Dayside (local noon ± 3hr) data are used.

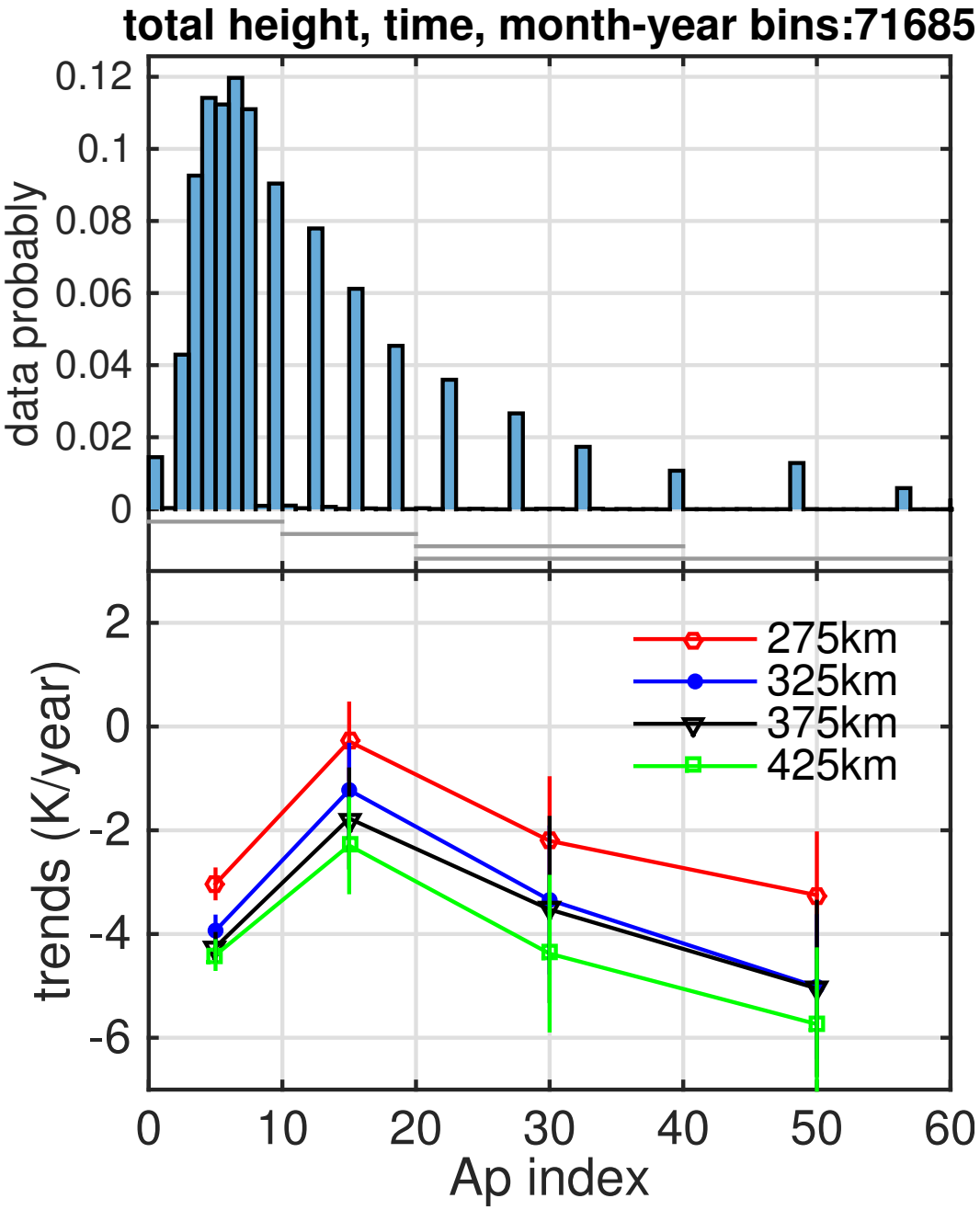

Figure 11. Sondrestrom T_i trends in the same manner as Figure 10 but as a function of Ap index.

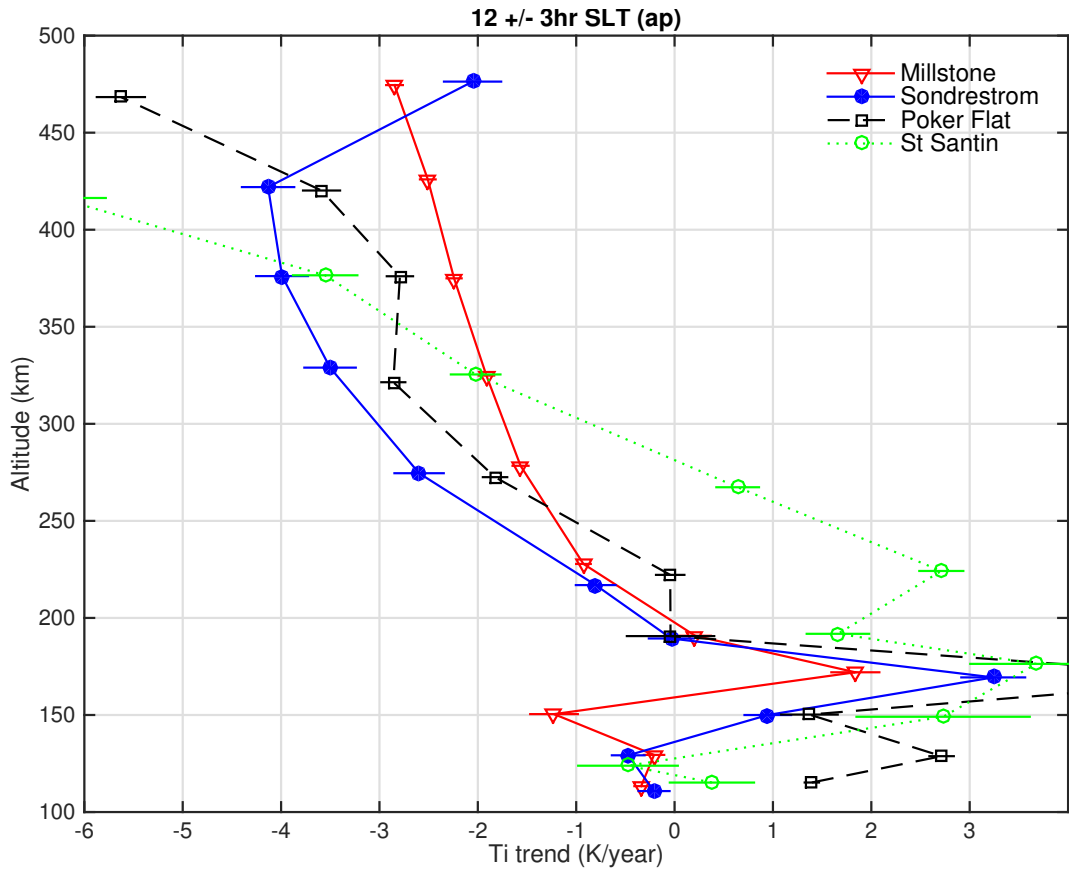

Figure 12. Dayside T_i trend profile comparisons among incoherent scatter radar observation sets at Millstone Hill (red solid), Chatanika/Poker Flat (dashed black), and Sondrestrom (blue solid). Corresponding St. Santin results (green) are shown for reference.

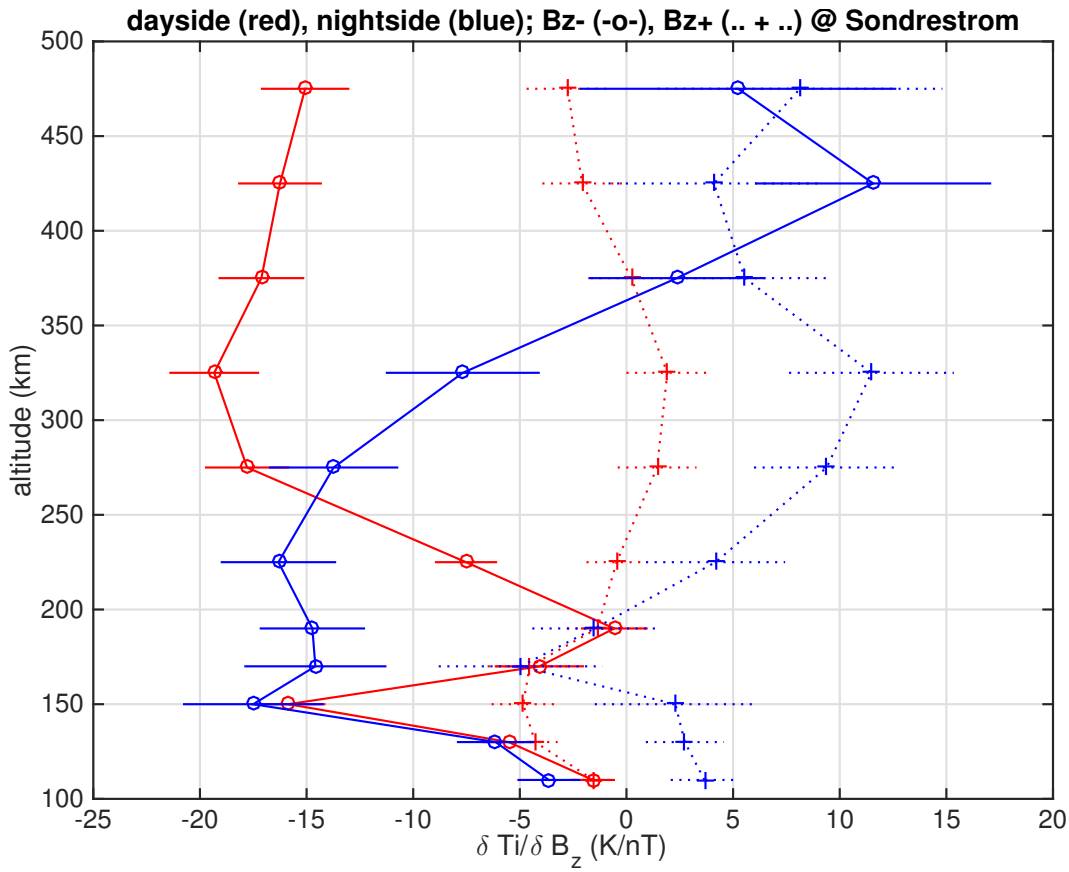

Figure 13. Sondrestrom altitude profiles of $\delta T_i/\delta Bz$, highlighting T_i responses to IMF Bz - (southward, circles) and Bz + (northward, crosses) on the dayside (red) and nightside (blue)

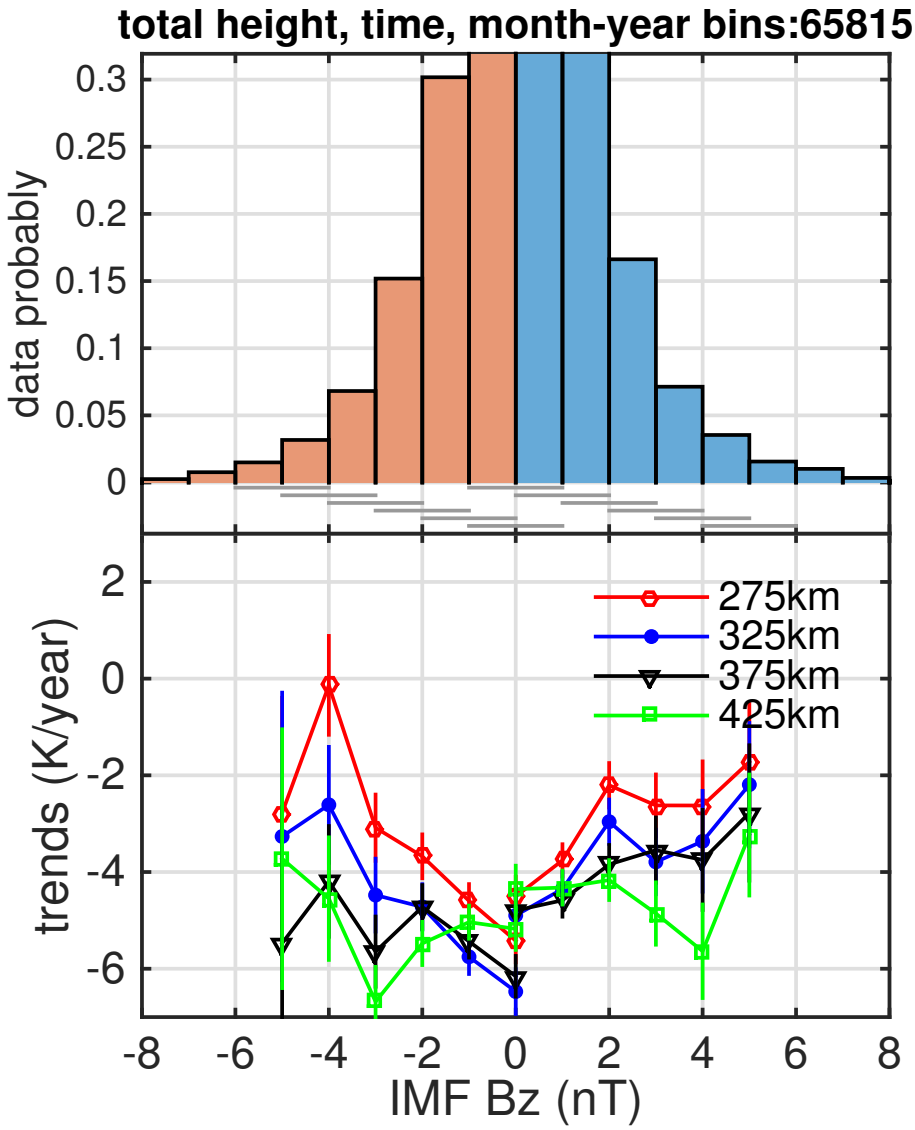

Figure 14. Sondrestrom altitude profiles in the same manner as Figure 10 but for IMF Bz dependency. Data with Bz+ ([0 10 nT]) and Bz - ([-10 0nT]) are analyzed separately each using the same analysis approach as for Ap. Results for both Bz + and Bz - are combined to produce the two panels.

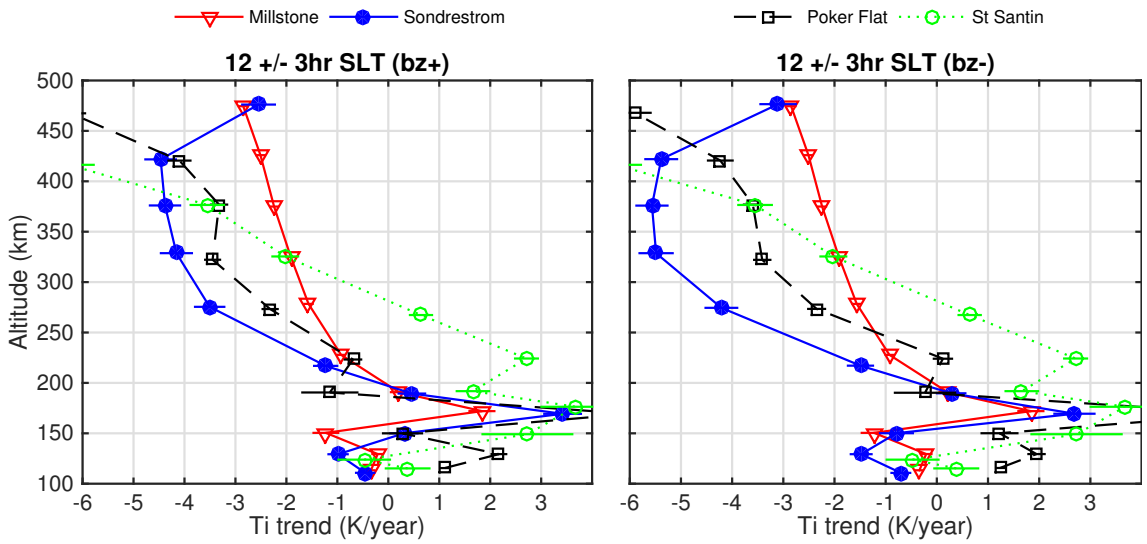

Figure 15. Comparisons of derived trends at noon for the incoherent scatter radar observation sets at Millstone Hill (red), Chatanika/Poker Flat (black), Sondrestrom (blue) and St. Santin (green). Data is organized in the same way as in Figure 12, except that results for Sondrestrom and Chatanika/Poker Flat are derived with Bz+ (left) and Bz - (right) respectively.